

# Anatomical and Gene Expression Changes in the Retinal Pigmented Epithelium Atrophy 1 (rpea1) Mouse: A Potential Model of Serous Retinal Detachment

Gabriel Luna,<sup>1,2</sup> Geoffrey P. Lewis,<sup>1,2</sup> Kenneth A. Linberg,<sup>1</sup> Bo Chang,<sup>3</sup> Quiri Hu,<sup>1</sup> Peter J. Munson,<sup>4</sup> Arvydas Maminishkis,<sup>5</sup> Sheldon S. Miller,<sup>5</sup> and Steven K. Fisher<sup>1,2,6</sup>

<sup>1</sup>Neuroscience Research Institute, University of California Santa Barbara, Santa Barbara, California, United States

<sup>2</sup>Center for Bio-Image Informatics, University of California Santa Barbara, Santa Barbara, California, United States

<sup>3</sup>The Jackson Laboratory, Bar Harbor, Maine, United States

<sup>4</sup>Mathematical and Statistical Computing Laboratory, Center for Information Technology, National Institutes of Health, Bethesda, Maryland, United States

<sup>5</sup>The National Eye Institute, National Institutes of Health, Bethesda, Maryland, United States

<sup>6</sup>Department of Molecular, Cellular and Developmental Biology, University of California Santa Barbara, Santa Barbara, California, United States

Correspondence: Steven K. Fisher, Neuroscience Research Institute, University of California Santa Barbara, Santa Barbara, CA 93106-5060, USA; fisher@lifesci.ucsb.edu.

GL and GPL contributed equally to the work presented here and should therefore be regarded as equivalent authors.

Submitted: December 29, 2015

Accepted: July 21, 2016

Citation: Luna G, Lewis GP, Linberg KA, et al. Anatomical and gene expression changes in the retinal pigmented epithelium atrophy 1 (rpea1) mouse: a potential model of serous retinal detachment. *Invest Ophthalmol Vis Sci.* 2016;57:4641–4654. DOI:10.1167/iovs.15-19044

**PURPOSE.** The purpose of this study was to examine the rpea1 mouse whose retina spontaneously detaches from the underlying RPE as a potential model for studying the cellular effects of serous retinal detachment (SRD).

**METHODS.** Optical coherence tomography (OCT) was performed immediately prior to euthanasia; retinal tissue was subsequently prepared for Western blotting, microarray analysis, immunocytochemistry, and light and electron microscopy (LM, EM).

**RESULTS.** By postnatal day (P) 30, OCT, LM, and EM revealed the presence of small shallow detachments that increased in number and size over time. By P60 in regions of detachment, there was a dramatic loss of PNA binding around cones in the interphotoreceptor matrix and a concomitant increase in labeling of the outer nuclear layer and rod synaptic terminals. Retinal pigment epithelium wholemounts revealed a patchy loss in immunolabeling for both ezrin and aquaporin 1. Anti-ezrin labeling was lost from small regions of the RPE apical surface underlying detachments at P30. Labeling for tight-junction proteins provided a regular array of profiles outlining the periphery of RPE cells in wild-type tissue, however, this pattern was disrupted in the mutant as early as P30. Microarray analysis revealed a broad range of changes in genes involved in metabolism, signaling, cell polarity, and tight-junction organization.

**CONCLUSIONS.** These data indicate changes in this mutant mouse that may provide clues to the underlying mechanisms of SRD in humans. Importantly, these changes include the production of multiple spontaneous detachments without the presence of a retinal tear or significant degeneration of outer segments, changes in the expression of proteins involved in adhesion and fluid transport, and a disrupted organization of RPE tight junctions that may contribute to the formation of focal detachments.

**Keywords:** retinal pigment epithelium, cell adhesion, retinal detachment, photoreceptors, extracellular matrix

The formation of a serous retinal detachment (SRD) is a component of many ocular conditions, including Vogt-Koyanagi-Harada syndrome, uveal effusion syndrome, various forms of ocular tumors, placoid pigment epitheliopathy, AMD, and particularly, central serous chorioretinopathy (CSCR).<sup>1–4</sup> Age-related macular degeneration and CSCR are the most notable because of the specificity to the human macula, the region of highest visual acuity. In SRD, fluid spontaneously accumulates between the RPE and neural retina creating an expanded subretinal space (SRS). Fluid leakage across the RPE from choroidal blood vessels (BV) into the SRS has been considered a primary driving force in the formation of CSCR.<sup>5–7</sup> Hyperpermeability of choroidal BV, regional death of RPE cells, and breakdown of junctional complexes between RPE cells

have all been proposed as mechanisms for the loss of retinal adhesion.<sup>5,7,8</sup> Active solute-linked fluid transport by the RPE from the SRS into the choroidal vasculature,<sup>9–11</sup> and molecular interactions between the RPE and photoreceptors have been described as mechanisms of normal retinal adhesion.<sup>12–14</sup> Thus, diseases involving SRD appear to require the buildup of fluid in the SRS in order to overwhelm multiple mechanisms underlying retinal adhesion.<sup>8</sup>

A SRD differs from the more common rhegmatogenous retinal detachment (RRD) in which a physical tearing of the retina allows vitreous to invade the SRS. The mechanism(s) in SRD remain speculative, little is known about its effects on the retina, and no suitable animal model exists. In 2008, a new mutant mouse strain (new mutant 3342, nm3342) now known

**TABLE 1.** A List of Antibodies and Probes Used in This Study

Antibody	Species	Dilution	Manufacturer	Catalog Number
Peanut agglutinin (PNA)	N/A	1:100	Vector Laboratories, Burlingame, CA	B-1075
anti-M/L opsin	rabbit polyclonal	1:500	EMD Millipore, Temecula, CA	AB5405
anti-ezrin	mouse monoclonal	1:5000	Sigma-Aldrich, St. Louis, MO	E8897
anti-aquaporin 1	rabbit polyclonal	1:100	EMD Millipore, Temecula, CA	AB3272
anti-cytochrome oxidase	mouse monoclonal	1:100	Molecular Probes-Invitrogen, Carlsbad, CA	A-6403
anti-E-cadherin	mouse monoclonal	1:100	BD Biosciences, San Jose, CA	610181
anti-beta-catenin	mouse monoclonal	1:500	BD Transduction Laboratories, Franklin Lake, NJ	610153
anti-occludin	rabbit polyclonal	1:100	Zymed Laboratories, San Francisco, CA	71-1500
anti-synaptophysin	rabbit polyclonal	1:100	DAKO, Carpinteria, CA	A-0010
anti-C-Terminal Binding Protein 2	mouse monoclonal	1:100	BD Transduction Laboratories, Franklin Lake, NJ	612044
anti-neurofilament	mouse monoclonal	1:500	Abcam, Cambridge, MA	ab8970
Hoechst 33342	N/A	1:5000	Molecular Probes-Invitrogen, Carlsbad, CA	H3570
<b>Secondary Antibodies</b>				
Donkey anti-rabbit	Cyanine Cy3	1:200	Jackson ImmunoResearch, West Grove, PA	711-165-152
Donkey anti-mouse	Alexa Fluor 488	1:200	Jackson ImmunoResearch, West Grove, PA	715-545-151
Streptavidin	Alexa Fluor 647	1:100	Jackson ImmunoResearch, West Grove, PA	016-600-084

as rpe1, was described in which spontaneous retinal detachments occur with no apparent physical tears in the retina (Chang B, et al. *IOVS* 2008;49:ARVO E-Abstract 5225). Observations in the mutant included shallow detachments by postnatal day (P) 60 with a progression until P120 when approximately 75% of the retina was detached. The genetic basis of this mutation was recently described, demonstrating a disruption of the *Prkcg* gene and that the protein was localized to the lateral surfaces of the RPE.<sup>15</sup> Thus, the rpe1 mouse may prove to be the first animal model for SRD and provide the basis for developing therapies for diseases in which that is a component. While some cases of chronic SRDs can be treated with photocoagulation or photodynamic therapy to seal “leaks” in the RPE,<sup>17</sup> the current standard of care in many cases of the most prevalent form of SRD, CSCR, can be described as “routine observation,” and usually the retina spontaneously reattaches with the episode of detachment resolving itself. However, even after successful reattachment of the retina and a return of vision in the 20/20 to 20/25 range, 40% of patients continue to report a variety of visual “symptoms,” and 60% report scotomas to blue light. Even episodes described as “mild” can have subtle and lasting effects on vision.<sup>5,16</sup> In 6% to 15% of cases, vision will continue to deteriorate to 20/200 or worse. Thus, even though most cases of CSCR may anatomically resolve spontaneously, it is not a visually benign condition.<sup>4</sup> Additionally, there are no readily accessible animal models of this or other forms of SRD. While a mouse cannot provide a model for foveal disease, the genetic strain examined here provides a convenient, readily available animal model in which the formation of spontaneous SRDs can be studied.

## METHODS

### Histology

Wild-type (WT) and rpe1 mice, both on the C57BL/6J genetic background, were euthanized with CO<sub>2</sub> on P30, P60, P90, P120, P180, P240, P365, and P730 ( $n = 4/\text{condition}/\text{age}$ ).

Optical coherence tomography (OCT) was performed prior to euthanasia. Following enucleation, the eyes were immersion fixed in 4% paraformaldehyde containing sodium phosphate buffer (0.1M; pH 7.4) for immunohistochemistry (IHC), or by intracardiac perfusion of buffered 1% glutaraldehyde and 1% paraformaldehyde for light and electron microscopy (LM, EM). All experimental procedures and use of animals followed protocols approved by the Animal Care and Use Committee of the University of California Santa Barbara, congruent with the Association for the Assessment and Accreditation of Laboratory Animal Care International (AAALAC).

### Animals

The characterization and isolation of the rpe1 strain is described in detail in Ji et al.<sup>15</sup> Briefly, the formation of retinal detachments was initially discovered in the murine ABJ/LeJ strain. In these mice, eyes appeared enlarged and displayed a large retinal detachment. However, the ABJ/LeJ strain carries two ocular mutations: asebia in stearyl-Coenzyme A desaturase 1 (*Scd1<sup>ab/f</sup>*) and retinal degeneration 1 in phosphodiesterase 6b (*Pde6b<sup>rd1</sup>*). Therefore, to remove these mutations mice were back-crossed with C57BL/6J mice for 10 generations (Chang B, et al. *IOVS* 2008;49:ARVO E-Abstract 5225).

### Immuno- and Lectin Histochemistry

Following fixation, immunocytochemistry was performed as described in detail elsewhere<sup>17,18</sup> and processed using primary antibodies, probes, and their corresponding secondary antibodies listed in Table 1. Slides were imaged using an Olympus FluoView 1000 laser scanning confocal microscope (Olympus, Inc., Center Valley, PA USA).

### Light and Electron Microscopy

Following initial fixation in Karnovsky’s fixative,<sup>19</sup> the tissue was postfixed in osmium tetroxide (2% in 0.086M PBS) for 1

hour, dehydrated in a graded ethanol series, and embedded in Spurr's resin (Electron Microscopy Sciences, Hatfield, PA, USA). The tissue blocks were sectioned using an ultramicrotome (Reichert-Jung Ultracut, Vienna, Austria) at 0.5 to 1  $\mu\text{m}$  for LM and 80 nm for EM. Subsequently, a JEOL JEM 1230 transmission electron microscope (Japan Electron Optics Laboratory, Tokyo, Japan) was used to capture EM micrographs.

### Western Blotting

Following removal of the cornea and lens, retinas were dissected and processed separately as either retina alone or with RPE and choroid as described elsewhere.<sup>20,21</sup> Blots were immunostained with primary antibodies to ezrin and aquaporin 1 overnight at 4°C. Membranes were then rinsed in PBS before being incubated in secondary antibodies (Molecular Probes, Eugene, OR, USA) for 1 hour at room temperature. Finally, samples were imaged using an Odyssey scanner (Li-Cor, Lincoln, NE, USA).

### Microarray

Wild-type and rpea1 mice at P30 and P365 ( $n = 4/\text{condition}/\text{age}$ ) were euthanized, after which time the mRNA was isolated from retina and RPE. Microarrays were performed by the Laboratory for Advanced Genome Analysis at the Vancouver Prostate Centre (Vancouver, British Columbia, Canada) as described in Massah et al.<sup>22</sup> To identify statistical significance fold changes were compared using a 2-way ANOVA. Here, significantly regulated genes were defined as genes with a  $P$  value less than or equal to  $10^{-4}$  and a fold-change greater than or equal to 2. Genes not annotated to an established gene symbol were omitted from this report. These genes were then analyzed further using Ingenuity Pathway Analysis (IPA) software (Ingenuity Systems, Redwood City, CA, USA). All genomic data have been deposited in the National Center for Biotechnology Information's (NCBI) Gene Expression Omnibus (GEO) and are publicly accessible through the GEO series accession number GSE68961.

### Quantitative Real-Time Polymerase Chain Reaction

Quantitative Real-Time Polymerase Chain Reaction (qRT-PCR) was performed to validate a subset of the microarray data as described elsewhere.<sup>23</sup> To account for variations, the data was normalized to the geometric mean of housekeeping genes with expression levels that do not change as a result of location, age, or disease.<sup>24</sup> Here housekeeping genes included: glyceraldehyde phosphate dehydrogenase (*Gapd*), hypoxanthine phosphoribosyltransferase (*Hprt*), glucuronidase beta (*Gusb*), peptidylprolyl isomerase A (*Ppia*), and TATA box binding protein (*Tbp*).

### Spectral-Domain Optical Coherence Tomography (SD-OCT) Imaging

Optical coherence tomography imaging was carried out in a manner described in Chen et al.<sup>25</sup> Briefly, SD-OCT images were obtained in mice observed to have developed SRD using the Bioptigen Spectral Domain Ophthalmic Imaging System (Bioptigen Envisu R2200, Morrisville, NC, USA). Image acquisition software was provided and supported by the vendor. Averaged single B-scan and volume scans were obtained using the optic nerve head (ONH) as an anatomical landmark for orientation.

## RESULTS

Optical coherence tomography imaging of rpea1 mice revealed areas of shallow detachments beginning at P30 (Fig. 1A), with

an increase in size, number, and height over time (Fig. 1B). Light microscopy of P30 animals confirmed the presence of small, shallow detachments (Fig. 1C; brackets) underlain by mostly intact outer segments (OS). Histologically, detachment extent and height increased with age, although most OS remained relatively long, their apical ends appeared disorganized (Figs. 1D, 1E). In some detached regions, the width of the OS layer remained normal but most of the OS appeared structurally disrupted (Fig. 1D). The large number of macrophages present in these detached regions was distinctive (Fig. 1F; arrows) indicating that the retina had been detached prior to euthanasia. Electron micrographs of attached regions in the mutant showed OS with bent or distorted tips. Notably, the RPE apical microvilli abutted the OS rather than extending between them (Fig. 1G). Electron microscopy revealed in more detail, distortion of the OS in areas of detachment and shorter, sparser, and even missing microvilli on the RPE apical surface (Figs. 1H, 1I).

The width of the OS layer was measured using LM sections in regions categorized as attached, shallowly detached, or deeply detached. At P30 in the rpea1 mice, the width of the OS layer was equivalent to that in WT animals ( $\sim 30 \mu\text{m}$ ). After that time, there was generally a decline in the width of the OS layer but with so much variability, even within a single histologic section, that we did not find a reliable way to obtain, systematic data even within one animal. The dilemma caused by this variability is illustrated by measurements from different animals. A single measurement was taken in an area of attached retina, and at the highest point of an area of detachment. In one mutant animal at P60 the width of the OS layer in attached retina varied between 30 and 40  $\mu\text{m}$  (the average for a normal adult mouse is generally accepted as 30  $\mu\text{m}$ ), in shallowly detached areas approximately 20  $\mu\text{m}$ , and in deeply detached regions 10  $\mu\text{m}$ . In another mutant at the same age, the OS width in attached retina averaged 35  $\mu\text{m}$ , while in deeply detached retina it was essentially the same, ranging from 30 to 40  $\mu\text{m}$ . A P180 mutant mouse had an OS layer width of 30  $\mu\text{m}$  in shallow and deeply detached retina and only 20  $\mu\text{m}$  in areas of attached retina. By P240 the width of this layer had declined overall but with variation between 10 and 20  $\mu\text{m}$  whether the retina was attached or deeply detached.

### Immuno- and Lectin Histochemistry

In WT retinas, biotinylated peanut agglutinin (PNA)-labeled extracellular matrix associated with cone OS (cone matrix sheaths), as well as with synaptic sites at the cone terminals (Fig. 2A; arrows).<sup>26</sup> In the shallow detachments that occur at P30, PNA labeling at the apex of the sheath sometimes appeared slightly fragmented (Fig. 2B) but otherwise normal; the labeling of cone pedicles appeared less distinctive (Fig. 2B; arrows) than in controls. In older animals PNA labeling decreased dramatically in the OS layer but appeared at greatly increased levels in the outer nuclear layer (ONL) as well as in small puncta in the synaptic terminal layer of the outer plexiform layer (OPL; Figs. 2C, 2D). Double labeling with PNA and C-terminal-binding protein 2 (CtBP2) of synaptic ribbons demonstrates that the small puncta in this synaptic layer are associated with invaginations of both rod and cone terminals (Fig. 2D); at P30 in the mutant and in control retina, PNA does not label the invaginations of rod terminals, only those of cones. Figures 2E and 2F demonstrate the variability in changes in PNA labeling within a single retina and also indicate a correlation between the degree of injury as indicated by increased anti-GFAP labeling of Müller cells and the decrease in the cone matrix sheath labeling with PNA.

Labeling with PNA (green) and anti-M/L cone opsin (red) was used to determine whether the OS of the cone population

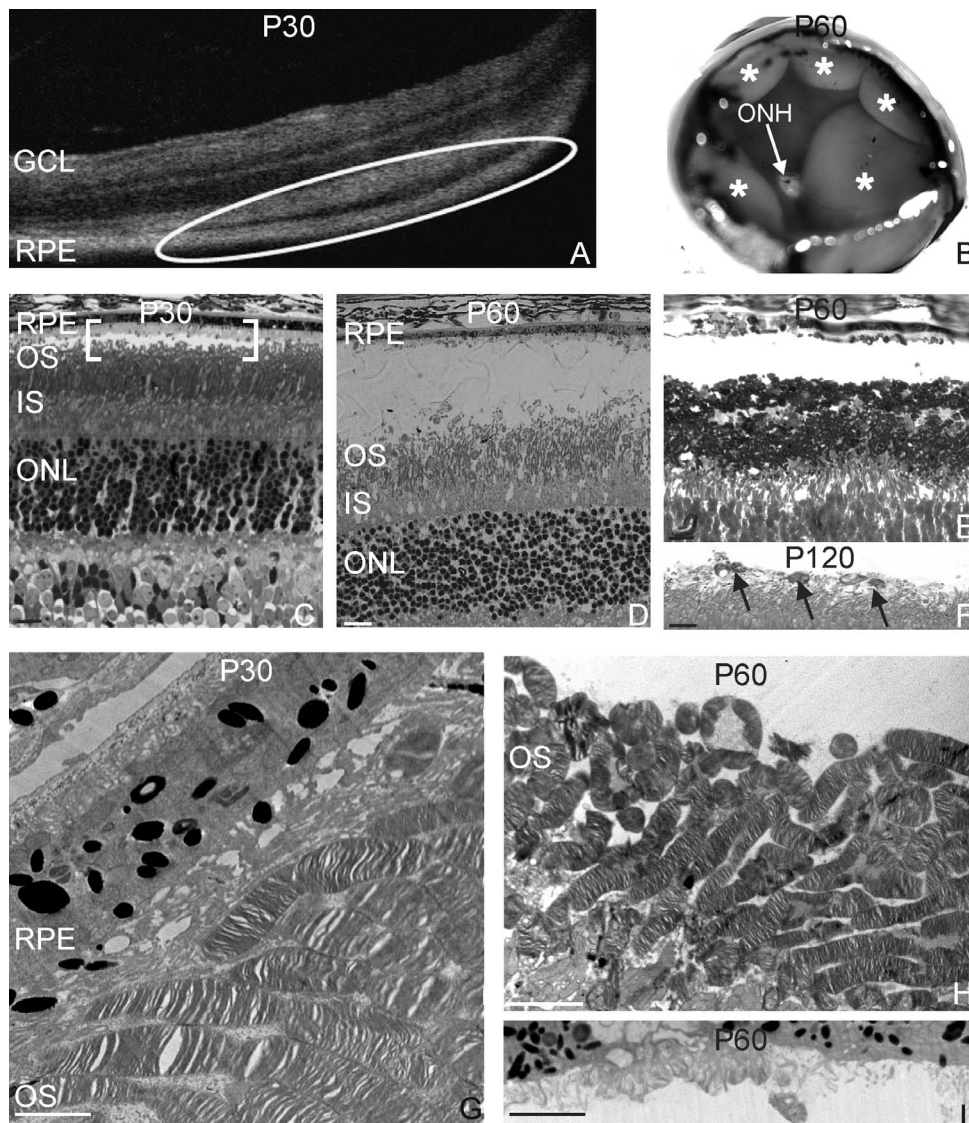
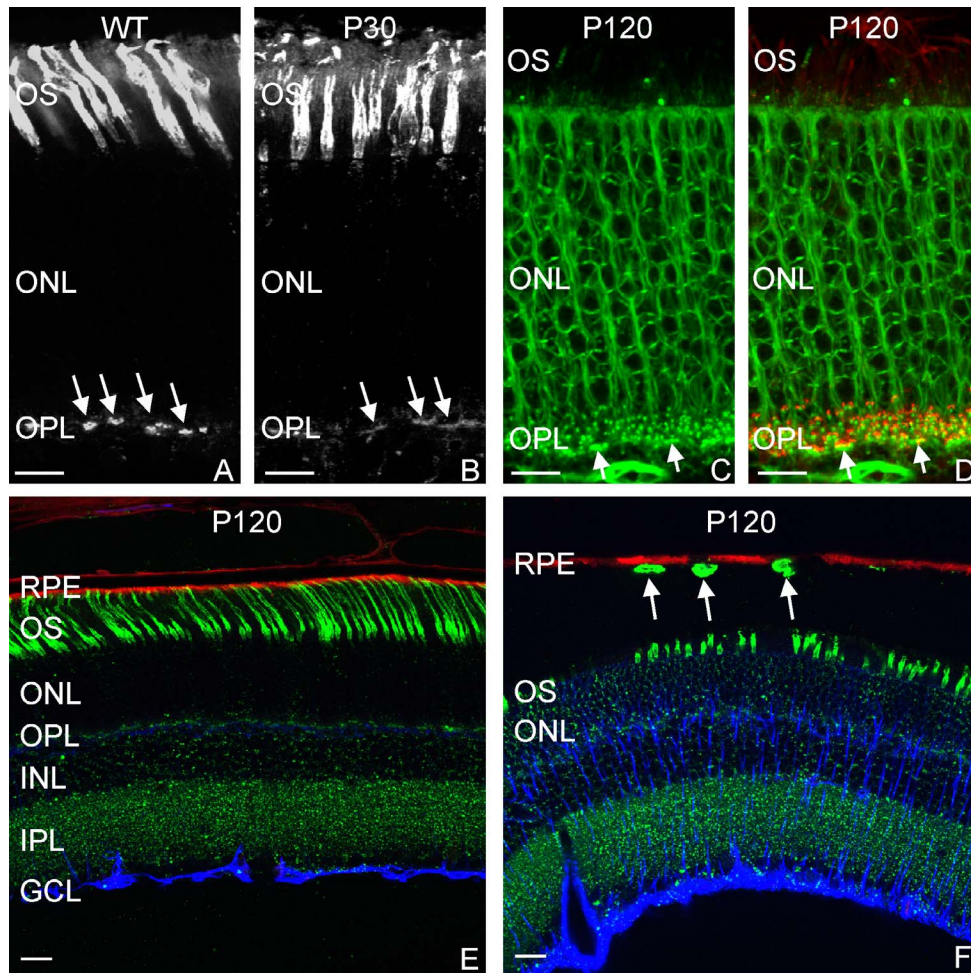


**FIGURE 1.** (A) Optical coherence tomography of a *rpe1* mouse eye showing a shallow detachment at P30 (*circled*). (B) Fundus photograph of an eyecup from a *rpe1* mouse illustrating multiple retinal detachments of varying size and depth (*asterisks*) amid attached regions at P60. (C) A focal shallow retinal detachment (*brackets*) with mostly intact OS at P30. (D–F) In deeper detachments at P60 and P120, the OS remain relatively long but show varying degrees of disorganization. Macrophages are typically present among the OS in the detached regions (*arrows*, F). (G–I) Electron micrographs of the *rpe1* mouse retina at the RPE–OS interface. (G) Attached retina in regions with relatively normal length OS, although their tips are distorted, disrupting their parallel arrangement. Retinal pigment epithelium apical microvilli appear to merely abut the OS rather than extend between them. (H) Detached retinal region showing long but less parallel OS. (I) Detached retinal region showing short or absent RPE apical microvilli (*arrows*). Scale bars: 20 (C–F), 2 (G), and 4  $\mu\text{m}$  (H, I). GCL, ganglion cell layer.

was affected by the absence of a cone matrix sheath (Fig. 3). Regions associated with an underlying detachment (shown by the presence of macrophages in the SRS of wholemounts, arrows; Figs. 3A, 3C) showed a sparse population of cone outer segment (COS) using an anti-cone opsin antibody by comparison to the large surrounding area of attached retina where the labeling intensity and general population of COS resembles that in WT animals (Fig. 3A). Thus, in attached retina the COS were robust with anti-cone opsin labeling, and always surrounded by a cone matrix sheath (Figs. 3B, 3D), while in regions of detachment the matrix sheath was lost, cone density was sparse, and the remaining COS appeared structurally irregular (Figs. 3C, 3E). Furthermore, COS clearly survived even in areas of detachment, however, by P60 and later, they were not surrounded by a matrix sheath, fewer in number, and

displayed a distorted appearance. Figure 3E, also reiterates the abnormal labeling of the ONL by PNA within a detachment.

Observations by LM and EM indicated that RPE apical microvilli are abnormally short in the mutant animals in general, and become shorter, sparser, or even absent on some RPE cells in regions of detachment. In WT animals, anti-ezrin labeling appeared as a continuous carpet of microvilli across the RPE (Fig. 4A). In *rpe1* mice, ezrin labeled microvilli were absent in a subset of cells, or reduced sufficiently to reveal the lateral margins of individual cells (Fig. 4B). Hoechst-stained nuclei were still present in the areas lacking ezrin labeling indicating the presence of RPE cells. Anti-ezrin labeling also revealed an apparent structural inversion of some RPE cells with ezrin-positive microvilli appearing on the basal side (Figs. 4C, 4D). In WT RPE, anti-aquaporin 1 labeling also appeared uniform across the apical surface (Figs. 4E, 4F). Tilting the



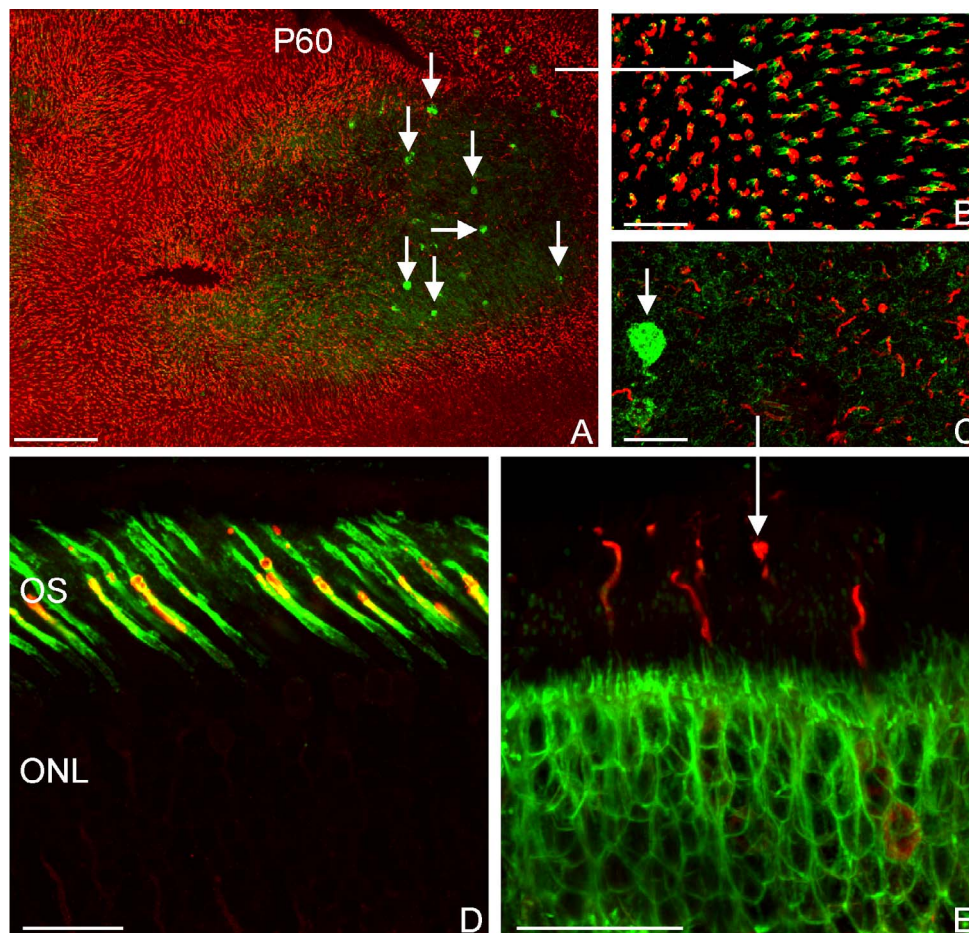
**FIGURE 2.** Confocal micrographs of PNA, anti-CtBP2, -ezrin, and -GFAP labeling in WT and *rpe1* retinas at varying postnatal times showing the loss of PNA from the IPM and its increase in the ONL and rod synaptic terminals of the mutant. (A) In WT retinas, PNA-labeled long, organized cone matrix sheaths as well as the matrix associated with the cone pedicles in the OPL (arrows). (B) At P30 in detached regions of the *rpe1* retinas, PNA labeling appeared fragmented at the tips of the cone OS, but otherwise had a similar distribution as in (A), although the labeling of cone pedicles (arrows) appeared less distinctive. (C) In a detached region of a P120 retina from the *rpe1* mutant, PNA labeling (green) decreased from the IPM, and increased in the extracellular space in the ONL. Peanut agglutinin labeling of the synaptic terminal layer of the OPL included a large number of small puncta as well as the still recognizable cone pedicles (arrows). (D) Double labeling with anti-CtBP2 (red) in synaptic ribbons, demonstrated that the PNA labeling was coincident with both the rod and cone synaptic terminals. ([C] is the same image as [D] without the anti-CtBP2 labeling to better visualize the PNA labeling of rod and cone terminals.) (E) In attached regions from a detached eye at P120, PNA (green)-labeled long, organized cone matrix sheaths, cone terminals in the OPL, and punctate areas of matrix in the IPL; anti-ezrin (red) labeled a continuous sheet of RPE that interdigitated the COS tips; anti-GFAP (blue) only labeled astrocytes in the GCL. (F) In detached regions within the same eye as shown in (E), PNA labeling of cone matrix sheaths showed varying degrees of truncation, and PNA labeling of the ONL also showed variability. Anti-GFAP strongly labeled the Müller cells indicating the retina was detached prior to fixation. Macrophages, labeled with PNA, are present in (F; arrows). Scale bars: 20  $\mu$ m.

image in Figure 4E revealed that the aquaporin 1 labeling occurred in a distinct band apical to anti-ezrin labeling (Fig. 4G). In the *rpe1* mice at P60, this labeling often became patchy across the RPE, but not necessarily coincident with that of anti-ezrin labeling (Figs. 4H, 4I). The differences become more apparent when the images are tilted (Fig. 4J). At P120, areas lacking labeling for both proteins are larger than at earlier ages (Figs. 4K–M).

A decrease in the expression of ezrin in the mutant RPE was confirmed by Western blot data showing a reduction at P30 with a further decrease at P365 that probably represents the significant loss of apical microvilli as detachments increase in the older animals (Fig. 5). Neither ezrin nor aquaporin 1 gene expression were significantly reduced in our microarray data, thus the decreases in protein expression

we observed probably represent changes in synthesis, trafficking or degradation.

In areas sclerad to detached retina, choroidal BV in the mutant animal appeared abnormally large and had thickened walls compared with WT animals (Figs. 6A, 6B). Interestingly, they also heavily labeled with anti-ezrin in the mutant (Figs. 6C, 6D), but never in WT animals. The disrupted pattern of anti-ezrin labeling of the apical RPE indicates that the abnormal BV's underlie regions of detached retina (Fig. 6D). Labeling of two adherens junction proteins, anti- $\beta$ -catenin and -E-cadherin as well as the tight-junction protein occludin in the WT RPE formed a regular labeling pattern that outlined individual RPE cells (Figs. 6E–G), however, in the *rpe1* mice the lack of labeling appeared as small patches of a few affected cells, or as extensive areas (Figs. 6H–J). These data demonstrate an apparent regionalized breakdown in the localization of both



**FIGURE 3.** Confocal micrographs of photoreceptors, shown in wholemount and in radial orientation, labeled with anti-M/L cone opsin (*red*), and PNA (*green*); the latter labels the cone matrix sheath as well as macrophages in areas of OS degeneration, illustrating the regional differences in the density of cone OS and influx of macrophages in a detached region at P60 in the *rpea1* mouse. (A) Low magnification image (P60) showing on the *right*, a region of reduced cone opsin and cone matrix sheath labeling and PNA labeled macrophages (*small arrows*). (B) A higher magnification image of the attached region shown in (A); *long arrow*, illustrating the presence of PNA labeling associated with the cone OS. (C) Higher magnification of the detached region shown in (A), illustrating the presence of a reduced number of cone OS that lack PNA-positive ensheathment. (D, E) Radial sections showing the presence of relatively long cone OS (*red*), associated with PNA labeled cone matrix sheaths in attached regions (D), but without such sheaths in detached regions (E). Note the increase in PNA labeling in the ONL in the detached region (E). *Smaller arrows* in (A, C) indicate macrophages labeled with PNA. Scale bars: 150 (A) and 20  $\mu$ m (B–E).

adherens and tight-junction proteins in the RPE of the mutant mouse. E-cadherin also labeled macrophages in the SRS in wholemounts, another indicator of an active immune response in the mutant (Fig. 6I; arrows).

In WT animals, intense immunolabeling with anti-cytochrome oxidase (COX), a marker for mitochondria occurred in the inner segments (IS) and synaptic terminals of the photoreceptors, with sparse labeling in the ONL (Fig. 7A). At P60, the number and size of labeled mitochondria were significantly increased in the ONL and the synaptic terminals, and the pattern of anti-COX labeling revealed an uneven, disorganized appearance of the photoreceptor synaptic terminal layer (Fig. 7B), similar to that observed by anti-CtBP2 labeling in Figure 2C. Labeling with anti-COX and -M/L cone opsin demonstrated that the abnormal anti-COX labeling pattern occurs in cones as well as rods (Figs. 7B, 7C), but is not limited to photoreceptors, occurring in the RPE (Fig. 7E) and inner retina (data not shown) as well. Labeling with anti-synaptophysin, -CtBP2 and -neurofilament revealed the retraction of photoreceptor synaptic terminals into the ONL and neurite sprouting from horizontal cells (data not shown) as has been described in experimental RRD.<sup>27</sup>

### Microarray Analysis

Genomic analysis identified genes differentially expressed in the *rpea1* mouse at P30 and P365 compared with age-matched WT animals. Thus, experiments contained two variables, the presence or absence of the mutation, and age. Forty-two genes met the criteria of at least a 2-fold change and a statistical value of  $P$  less than or equal to  $10^{-4}$  in the 2-way ANOVA that were attributed to the mutation alone. The majority of genes significantly affected by the mutation cluster on chromosome 11. Table 2 lists the 31 genes that were significantly upregulated and the 11 genes that were significantly downregulated. Figure 8A includes a heat map to compare results from the mutant and WT animals, while the graphs show the values for clustered genes at P30 and P365. Genes encoding the amylases, *Amy1* and *Amy2a5*, showed a greater decrease in expression at P30 than at P365 (Fig. 8A; cluster 8), while the *Calca* gene, showed the largest increase in expression at P365; the largest downregulation occurred for *Amy1*, and *Agxt211* at P30.

Nine genes associated with a cellular signaling and/or regulatory function showed significant changes. Of these, *Clnka*, a transmembrane voltage-gated chloride channel,

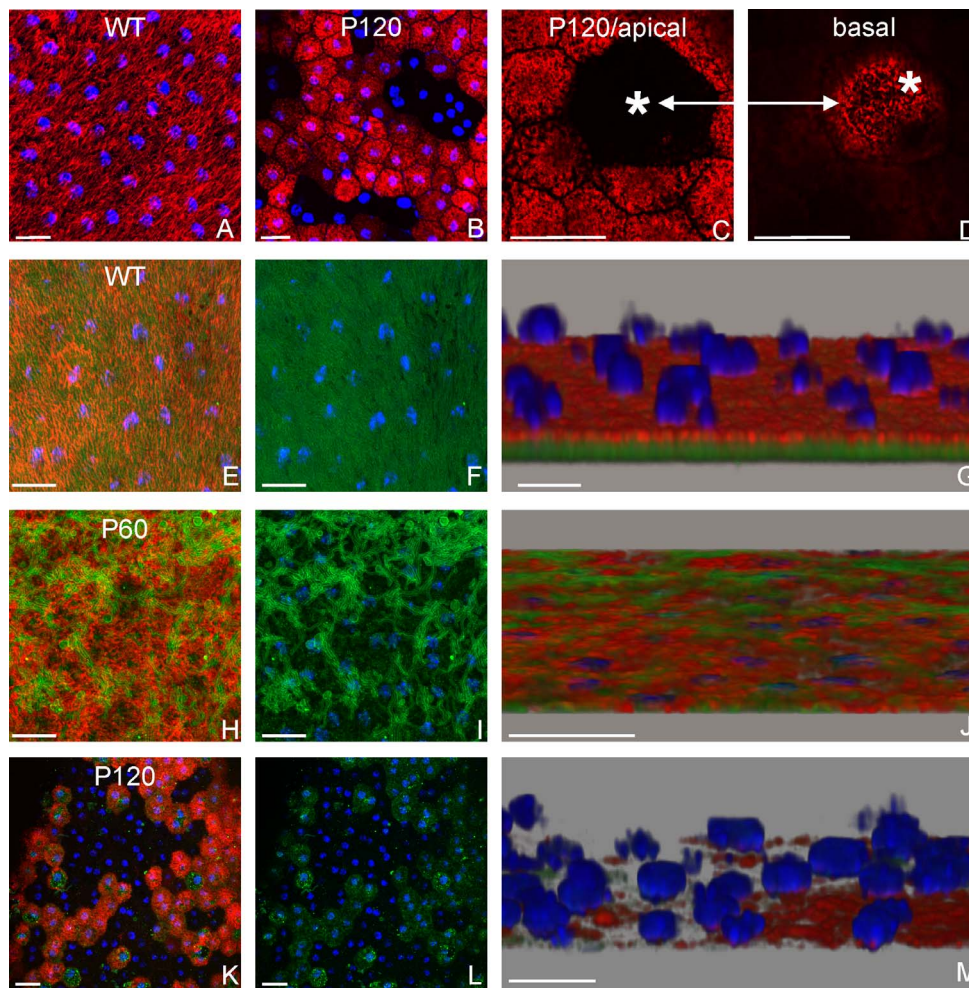


**FIGURE 4.** Confocal micrographs of anti-ezrin (*red*) labeling of whole-mounted RPE in WT and *rpe1* mice at P120 depicting a patchy loss of ezrin in the mutant mice. **(A)** In WT mice, anti-ezrin labeling appeared as a continuous sheet of microvilli across the surface of the RPE. **(B)** Low magnification view of the patchy labeling patterns in the *rpe1* mice. Anti-ezrin labeling was reduced overall, allowing the visualization of microvilli as small punctate structures and the lateral margins of single RPE cells. In some cells the labeling is missing altogether. **(C, D)** Images at two different focal depths in the confocal z-stack of the cell marked with an *asterisk*. Anti-ezrin labeling of the microvilli in this cell shifts from its typical localization on apical surface to the basal surface. Hoechst-stained nuclei (*blue*) in **(A, B)** illustrate that the absence of anti-ezrin staining is not due to cells missing from the monolayer. **(E–G)** Confocal micrographs showing anti-ezrin (*red*) and anti-aquaporin 1 (*green*) labeling of whole-mounted RPE from WT and *rpe1* mice revealing that the expression of both proteins decreases in the mutant animals, but not in overlapping patterns. Hoechst-stained nuclei are shown in blue and extend more basally in relation to the apically located proteins. In WT RPE, both proteins appear uniformly localized to the apical surface. **(G)** Shows a tilted view of **(E)** illustrating that anti-aquaporin 1 labeling is apical to the ezrin labeling in the apical microvilli, and both are evenly distributed. **(H–J)** The anti-ezrin- and -aquaporin 1-labeling patterns in the *rpe1* mice at P60, appears patchy across the RPE. **(J)** A tilt of the image shown in **(H)** and illustrates that the loss of labeling for these proteins does not necessarily overlap nor occur in any easily recognized pattern. Only the apical edge of the nuclei are included in this image to better visualize the ezrin and aquaporin 1-labeling patterns. **(K–M)** Labeling patterns in *rpe1* mice at P120, the loss of ezrin and aquaporin 1-labeling is more severe than at P60. **(M)** A tilt of **(K)**. Note that there are areas in which both proteins appear to be absent, some areas labeled only for ezrin (*red*), and some only for aquaporin 1 (*green*). Overall, aquaporin 1 expression appears to be affected more than that of ezrin. Scale bars: 20  $\mu\text{m}$ .

showed the greatest average change. Upregulation of the endothelin 2 (*Edn2*) gene at P365 showed the greatest single change in the group. Increased expression of the *Edn2* gene has been described in many retinal degenerative conditions, including experimental RRD.<sup>28,29</sup> Endothelin 2 is considered a vasoconstrictive peptide, but in the retina it also appears to be expressed by photoreceptors and activates a neuroprotective feedback pathway for photoreceptors.<sup>28</sup> The *Prkcc* gene encodes a Ser/Thr kinase, and was the third most downregulated gene. By qRT-PCR this gene was undetectable in the mutants (Table 2), supporting previous observations that PKC theta was undetectable at the protein level.<sup>15</sup> The gene showing the largest decrease in expression was *Pard3*, a gene

involved in regulating cell polarity and the formation of junctional complexes.

Seven genes associated with the inflammatory/immune response were upregulated in mutant mice, none were downregulated, and all belong to clusters that show an upregulated trend with age (Fig. 8A; clusters 1, 2, 4, 5). Among these genes, *Retnla*, a cytokine associated with responses to hypoxia, showed the greatest upregulation.

Four cytoskeletal-associated genes demonstrated increases in the mutant, most prominently, *Krt23*, a gene expressed by epithelial cells. Keratins are known to be expressed by the RPE and are involved in responses to cellular stress, including mechanical stress.<sup>30</sup> Keratin 18, a paralog of keratin 23, increases expression in migratory RPE cells.<sup>31</sup> An increased

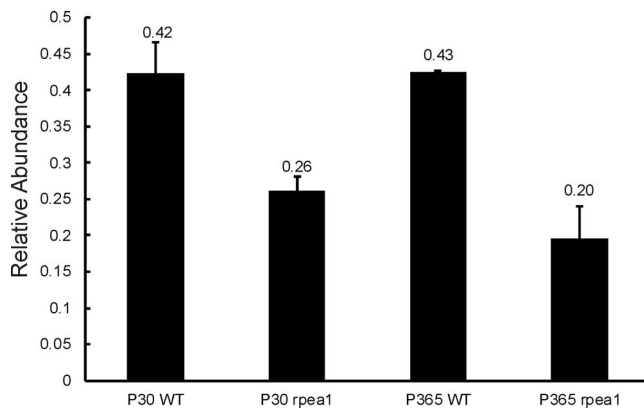


**FIGURE 5.** Western blot graph of the densitometric scan showing an almost 2-fold loss of ezrin from the RPE in rpea1 mice compared with WT mice at P30 and P365. Error bars represent standard error of the mean ( $n = 3$ ).

expression of cytokeratin may reflect the RPE's response to the stress of the spontaneous detachments.

Three extracellular matrix associated genes (*ADAM7*, *Postn*, *Col3a1*) were upregulated in the mutant, while two were downregulated (*Adamts18*, *Omg*). *ADAM7*, encodes a disintegrin and metallopeptidase domain 7 protein with poorly understood roles in cell-cell adhesion and migration, while other members of the *ADAM* gene family are differentially expressed in the inner retina during development.<sup>32-34</sup> Interestingly, the lack of expression of *ADAM9* produces a retinal degeneration in canines associated with a lack of apical microvilli on RPE cells.<sup>35</sup> Increased periostin (*Postn*) expression in retina is associated with proliferative diseases involving  $\alpha$ -V/ $\beta$ -3 integrin, including diabetic retinopathy.<sup>36</sup> Collagen type III (*Col3a1*) showed the greatest upregulation at P30, supporting our histologic observations of increased size and thickness of choroidal BV underlying the detachments (Figs. 6B, 6D).

The increased expression of *Bcl2l15* is the only significant change in a gene associated with apoptosis in the mutant. While apoptotic cells were occasionally identified among photoreceptors in the mutants, their numbers were small, and there was no obvious change in width of the ONL even in areas of detachment, suggesting that cell death may not be a major event, in agreement with Wu et al (*IOVS* 2009;50:ARVO E-Abstract 4494).

The most striking differences between the qRT-PCR and microarray data occurred for the expression of the *Prkccq* and *Pard3* genes. *Prkccq* showed a significant downregulation in the microarray data, while undetectable by qRT-PCR. *Pard3* showed the greatest single change among downregulated genes in the microarray data, with downregulation at P365 by qRT-PCR. *PRKCCQ* and a cluster of three *CCL* genes are each involved in nine of the top 20 canonical pathways predicted to be affected in the rpea1 mouse (Table 3). The *PARD3* gene is involved in three such pathways. Figure 8B illustrates the gene network predicted to be affected by the downregulated genes in the microarray data. The network demonstrates the wide-ranging effects of these downregulated genes, but with two major gene foci: ubiquitin C and *PARD3*, with the latter acting as a key regulator of asymmetrical cell division, cell polarity, and tight-junction formation (GeneCards).<sup>37</sup>

## DISCUSSION

Data from a mouse that produces SRD may provide clues for future studies of molecular mechanisms in human diseases

with SRD and provide a basis for the development of new therapeutic strategies. The goal of this project was to determine if the rpea1 mouse may serve as a model system, and a source of information relevant to human SRD. We applied a battery of techniques to make this determination, and in general believe the data largely supports both. Structural changes in the choroid-RPE-retina resemble those reported in cases of CSCR, a poorly understood and fairly widespread condition whose most prominent characteristic feature is SRD. Gene expression changes in this mutant are highly complex and broad in their scope, however, they may be highly relevant to the formation of SRDs. Results here present a short-list of gene changes that point to important cellular mechanisms that may be operative in producing SRDs in humans.

When characterizing the anatomic changes that occur in the rpea1 mouse, we observed that extensive detachments are present as early as P30 in this strain. These early detachments appeared varied in both their extent and depth, often widespread across the retina. Additionally, abnormal expression of ezrin and junctional complex proteins in the RPE were observed at P30 associated with the detachments and not observed outside areas of detachments. In the rpea1 strain, we observed abnormal choroidal BV's in P60, but not in P30 animals indicating that this change is delayed relative to the formation of detachments. The novel redistribution of PNA, a lectin that labels the matrix sheath around COS, into the ONL is evident at P60, not at P30. In general, some photoreceptor outer segment degeneration occurs but is highly variable, not occurring systematically with retinal region or age. By contrast, the degeneration of ROS and COS and deterioration of the cone matrix sheath occurs within days of the formation of a rhegmatogenous detachment, another indication that detachments caused by this mutation differ significantly from detachments in which there is a tear through the retina.

In other studies of this same mutant, (Chang B, et al. *IOVS* 2008;49:ARVO E-Abstract 5225; and Wu DM, et al. *IOVS* 2009;50:ARVO E-Abstract 4494) reliable detachments were reported only to be found in P60 animals. Additionally, OCT data and observations of dissected eye-cups show that the detachments form without physical tearing of the retina, then progress in size, number, and depth with age. Thus, the detachments most likely form by spontaneous accumulation of subretinal fluid. Although both ROS and COS often appear structurally disrupted and shorter in some areas of detachment, the OS layer does not completely degenerate and often appears relatively normal within a detachment. At P60 and later, choroidal BV adjacent to and underlying the SRD appear enlarged and thickened and abnormally express the cytoskeletal protein ezrin. Abnormal choroidal vessels also occur in the human disease CSCR, although in neither case is the relationship between the abnormal vessels and the mechanism of retinal detachment clear. Indeed in our observations these abnormal vessels are absent at P30, a time when early detachments appear in the mutant. These events all represent major differences with RRD.<sup>38-40</sup> There is also evidence that spontaneous reattachment may occur in these mice because of observed areas of attached retina that had disrupted OS and an increased expression of GFAP in Müller cells, the latter a highly sensitive indicator that the area had been previously detached. A more comprehensive approach to validating this conclusion could be accomplished by serial high-resolution OCT imaging of these mice as they age. Such a study would further support the conclusion that the molecular mechanisms in play in the rpea1 mouse are similar to other conditions involving SRD.

Anatomically, retinas in these mice may only be loosely attached to the RPE from birth, a conclusion supported by the fact that at P30, OS merely abut abnormally short apical processes, rather than interdigitate with them and the fact that



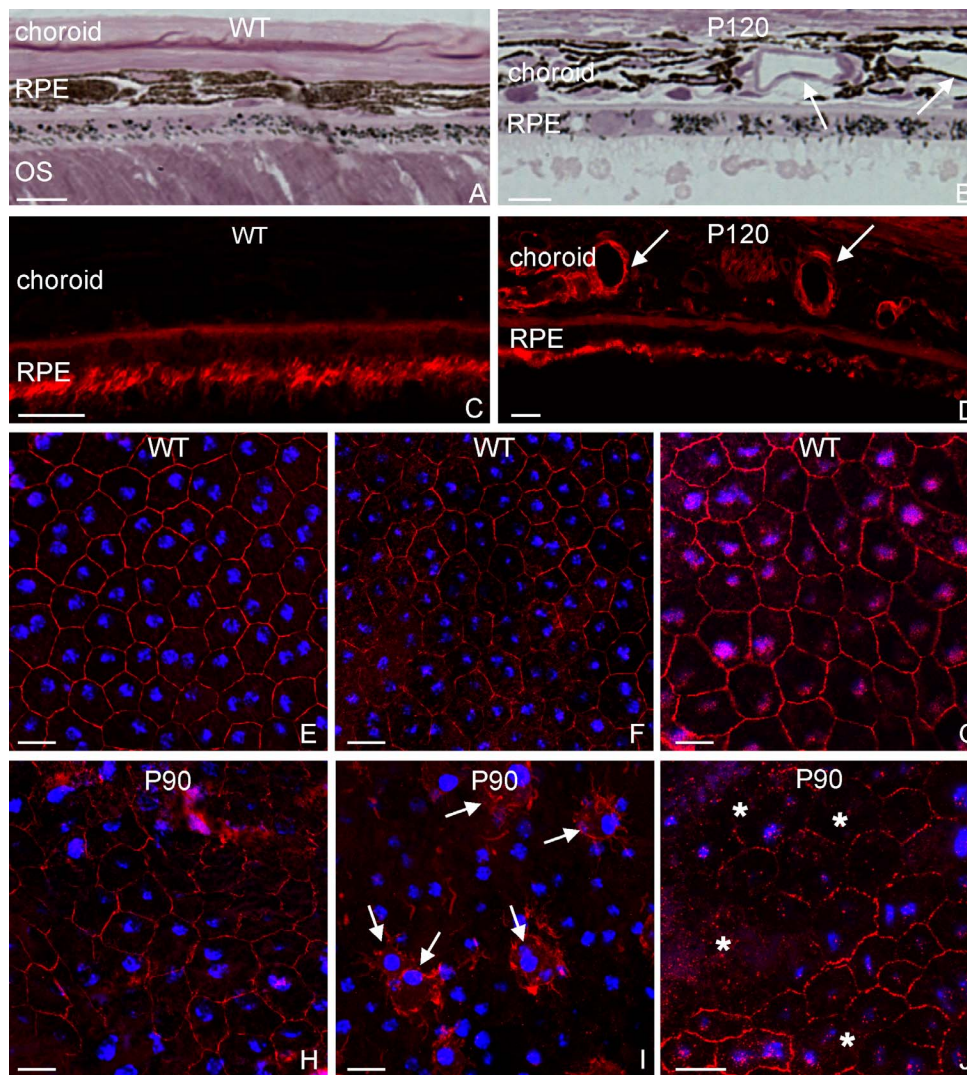


**FIGURE 6.** Images illustrating the enlarged choroidal vessels observed underlying detachments in the rpea1 mice. (A, B) Light micrographs of WT (A) and rpea1 mice (B) at P120 showing the increased size of the choroidal vessels (arrows) in an area of detachment. (C, D) Confocal images of sections from WT (C) and rpea1 mouse eyes at P120 (D) labeled with anti-ezrin (red) illustrating the enlarged choroidal vessels observed in areas of detachment (arrows). The apical microvilli also appear shortened with areas of disruption in the rpea1 mouse (D), typical of detached areas. Confocal micrographs of anti- $\beta$ -catenin (E, H) and -E-cadherin (F, I) and -occludin (G, J) labeling of whole-mounted RPE in WT and rpea1 mice at P90. (E–G) In WT RPE, labeling of these proteins is present in adherens junctions located at the lateral margins of the cells. (H–J) In rpea1 mice, this labeling can appear disrupted (J, asterisks), illustrating the irregular shape of the cells (H), or completely absent from the lateral margins (I). E-cadherin also labels macrophages on the surface of the RPE in (I, arrows). Scale bars: 20  $\mu$ m.

very shallow detachments occur often at this time. A reduced synthesis of the core molecule in the interphotoreceptor matrix (IPM) recognized by PNA has been shown to produce small retinal detachments,<sup>41</sup> suggesting a role in retinal adhesion. The collapse of the cone matrix sheath and a shift in PNA labeling to the ONL in the mutant may contribute to a weakening of retinal adhesion and the formation of the SRD. Alternatively, this observation may arise as a product of SRD formation, although data from studies of induced RRD suggest this is unlikely.<sup>26</sup>

The observed abnormal apical microvilli, and abnormal patterns of ezrin and aquaporin 1 expression may all indicate that the mutation may severely affect the ability of these animals to regulate the polarity of RPE cells.<sup>42–46</sup> All of these may be attributed to the effects of downregulation in the mutant of the *Prkccq* and *Pard3* genes with their roles in establishing cell polarity. None of the observed changes in labeling patterns with PNA, anti-ezrin, or anti-aquaporin 1, nor

changes in RPE cell structural polarity have been reported for experimental RRD, suggesting that they are not caused by detachment, but are a product of the mutation and likely contribute to the formation of the SRDs.

Abnormality of the choroidal BV is increasingly accepted as a major component of CSCR.<sup>5</sup> Wu et al (*IOVS* 2009;50:ARVO E-Abstract 4494) described leakage from retinal microvessels in a subset of rpea1 mice but did not report leakage from choroidal vessels or across the RPE. Although focal regions of fluorescein leakage across the RPE is sometimes observed in human CSCR, its appearance is inconsistent and often difficult to detect. We observed regions of abnormal choroidal BV in the older mutant mice but did not find these in animals with detached retinas at P30. Both the upregulated *CCL12* and *Col3a1* genes are predicted to have effects on the vasculature. An increased production of collagen type III by endothelial cells may also explain the abnormal thickness of the walls of choroidal BV in the mutant. These data suggest that the mutation does affect

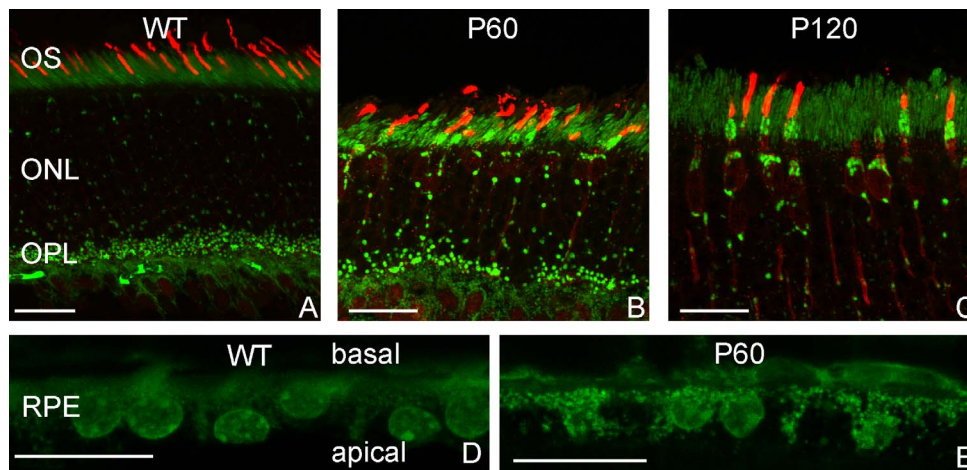


**FIGURE 7.** (A–E) Confocal micrographs of anti-COX (green) labeling illustrating the increase in number and size of mitochondria in the rpea1 mice; anti-M/L cone opsin (red) shows the location of cone OS. (A) In WT retina, anti-COX labels the numerous small mitochondria normally present in the photoreceptor IS and synaptic terminals in the OPL. Mitochondria are sparse in the ONL. (B, C) In retinas from the rpea1 mice at P60 and P120, anti-COX labeling shows a dramatic increase in the number and size of mitochondria, particularly in the ONL. Labeling with anti-cone opsin, which lightly labels the entire cone cell in detached regions, illustrates that many of the mitochondria are present in the cone photoreceptors as well as rods. (D, E) A comparison of anti-COX labeling in the RPE of WT and P60 mutant animals. As in the neural retina, there was an overall increase in labeling intensity in rpea1 mouse, indicating that the effect of the mutation on mitochondria is not specific to the retina. Scale bars: 2 (A, B) and 20 μm (C–E).

**TABLE 2.** A List of the 42 Genes That Met the Criteria of at Least an Average of a 2-Fold Change in Expression and a Significance Level of  $P \leq 10^{-4}$  as Calculated Using a 2-Way ANOVA That Includes Factors for Age and Mutation (Column 1), Chromosomal Location of the Gene, Whether qRT-PCR Data was Collected for the Gene, and the Probe ID on the Agilent Chip Used to Generate the Data

Gene Symbol	Gene Name	Average 2-way ANOVA with Interactions	Microarray Fold Change		qRT-PCR Fold Change		Chromosome Location	Functional Category	Agilent Probe ID
			1 Month	1 Year	1 Month	1 Year			
<b>Up-regulated</b>									
<i>Calca</i>	Calcitonin/calcitonin related polypeptide, alpha	2.37	0.74	7.76	1.08	2.80	7	Metabolism	A_55_P2139942
<i>Lalba</i>	Lactalbumin, alpha	2.18	1.47	3.25	N/A	N/A	15	Metabolism	A_55_P2150540
<i>Gox8b</i>	Cytochrome c oxidase, subunit VIIIb, nuclear gene encoding mitochondrial protein	2.69	1.92	3.52	2.97	2.35	7	Metabolism	A_55_P423814
<i>Sgsh</i>	N-sulfoglucosamine sulfohydrolase (sulfamidase)	2.06	2.29	1.02	3.36	2.14	11	Metabolism	A_55_P2028571
<i>Nnt</i>	Nicotinamide nucleotide transhydrogenase, nuclear gene encoding mitochondrial protein	2.04	1.92	2.17	2.14	2.20	13	Metabolism	A_55_P21144285
<i>Smek2</i>	SMEK homolog 2, suppressor of mek1 (Dictyostelium)	2.17	2.37	1.07	N/A	N/A	11	Signaling	A_55_P2058157
<i>Mctp1</i>	Multiple C2 domains, transmembrane 1	2.14	1.45	3.16	N/A	N/A	13	Signaling	A_55_P2016376
<i>Clcnka</i>	Chloride channel Ka, transcript variant 1	5.19	5.18	5.21	1.29	1.14	4	Signaling	A_55_P1976534
<i>Gbp3</i>	Guanylate binding protein 3	2.32	4.24	1.24	N/A	N/A	3	Signaling	A_55_P2472435
<i>Trim67</i>	Tripartite motif-containing 67	3.24	4.22	2.48	N/A	N/A	8	Signaling	A_55_P114528
<i>Gsg2</i>	Germ cell-specific gene 2	2.84	3.05	2.65	N/A	N/A	11	Signaling	A_51_P151586
<i>Edn2</i>	Endothelin 2	4.94	1.45	16.81	1.56	20.33	4	Signaling	A_51_P482121
<i>Ccl24</i>	Chemokine (C-C motif) ligand 24	2.00	2.57	1.55	3.85	1.71	6	Inflammatory/Immune	A_51_P328640
<i>Ccl28</i>	Chemokine (C-C motif) ligand 28	2.37	1.16	4.85	1.68	9.53	13	Inflammatory/Immune	A_55_P2175915
<i>Ccdc85a</i>	Coiled-coil domain containing 85A, transcript variant 3	2.35	2.06	2.67	N/A	N/A	11	Inflammatory/Immune	A_51_P101985
<i>Retna</i>	Resistin like alpha	3.47	7.03	1.72	N/A	N/A	16	Inflammatory/Immune	A_51_P257951
<i>Cue1p1</i>	CUE domain containing 1 (Cue1), transcript variant 1	4.23	3.98	4.49	N/A	N/A	11	Inflammatory/Immune	A_51_P379409
<i>Ccl12</i>	Chemokine (C-C motif) ligand 12	2.34	2.76	1.98	3.21	1.97	11	Inflammatory/Immune	A_55_P1984556
<i>Il1272a</i>	Interferon, alpha-inducible protein 27 like 2A	2.20	3.14	1.54	N/A	N/A	12	Inflammatory/Immune	A_52_P90383
<i>Myl4</i>	Myosin, light polypeptide	2.80	3.00	2.62	N/A	N/A	11	Cytoskeleton	A_55_P2107045
<i>GFAP</i>	Glial fibrillary acidic protein, transcript variant 2	2.40	1.54	3.74	1.58	4.64	11	Cytoskeleton	A_55_P2157250
<i>Tnni2</i>	Troponin T2, cardiac, transcript variant 9	2.19	1.57	3.06	N/A	N/A	1	Cytoskeleton	A_51_P338262
<i>Krt23</i>	Keratin 23	4.31	8.41	2.21	N/A	N/A	11	Cytoskeleton	A_51_P287198
<i>ADAM7</i>	A disintegrin and metallopeptidase domain 7	2.60	1.92	3.52	N/A	N/A	14	Extracellular Matrix	A_55_P2025735
<i>Postn</i>	Periostin, osteoblast specific factor, transcript variant 3	2.08	3.55	1.22	3.89	1.22	9	Extracellular Matrix	A_55_P1954086
<i>Col3a1</i>	Collagen, type III, alpha 1	2.42	5.02	1.07	6.25	1.10	1	Extracellular Matrix	A_51_P515605
<i>Bcl2l15</i>	BCL2-like 15, transcript variant 2	2.02	2.46	2.14	N/A	N/A	3	Apoptosis	A_55_P1975877
<i>Fam89a</i>	Family with sequence similarity 89, member A	2.02	1.92	2.14	N/A	N/A	12	Unknown	A_55_P2081116
<i>Dclre1b</i>	DNA cross-link repair 1B, PSO2 homolog (S. cerevisiae)	2.63	2.94	2.36	N/A	N/A	3	Unknown	A_55_P2128566
<i>Tlcd2</i>	TLC domain containing 2	2.71	2.94	2.51	N/A	N/A	11	Unknown	A_51_P328622
<i>Ankrd40</i>	Ankyrin repeat domain 40, transcript variant 2	2.03	2.52	1.63	N/A	N/A	11	Unknown	A_55_P2073121
<b>Down-regulated</b>									
<i>Amy1</i>	Amylase 1, transcript variant 1	-2.62	-4.12	-1.67	-3.77	-1.75	3	Metabolism	A_55_P1983418
<i>Amy2a5</i>	Amylase 2a5	-2.28	-3.71	-1.74	N/A	N/A	3	Metabolism	A_55_P2139402
<i>Egln1</i>	EGL nine homolog 1 (C. elegans)	-2.60	-2.27	-2.99	1.05	-1.07	8	Metabolism	A_51_P186899
<i>Gaa</i>	Glucosidase, alpha, acid, transcript variant 1	-2.56	-2.62	-2.62	N/A	N/A	11	Metabolism	A_55_P2024431
<i>Glxcl4</i>	Glyoxalase domain containing 4	-2.21	-2.15	-2.28	1.12	1.25	11	Metabolism	A_55_P2168058
<i>Agx12l1</i>	Alanine-glyoxylate aminotransferase 2-like 1	-2.57	-4.03	-1.64	N/A	N/A	3	Metabolism	A_51_P391616
<i>Per1</i>	Period homolog 1 (Drosophila), transcript variant 1	-2.03	-2.38	-1.74	N/A	N/A	11	Metabolism	A_55_P1970033
<i>Prkca</i>	Protein kinase C, theta	-3.20	-2.92	-3.50	ND	ND	2	Signaling	A_52_P72587
<i>Pard3</i>	Par-3 (partitioning defective 3) homolog (C. elegans), transcript variant 3	-10.84	-10.20	-11.52	1.01	-1.05	8	Signaling	A_55_P1985015
<i>Adams18</i>	Disintegrin-like and metallopeptidase (reprolysin type) with thrombospondin type 1 motif, 18	-2.03	-2.84	-1.56	N/A	N/A	16	Extracellular Matrix	A_51_P283968
<i>Omg</i>	Oligodendrocyte myelin glycoprotein	-4.95	-5.50	-4.46	N/A	N/A	11	Extracellular Matrix	A_55_P2105472

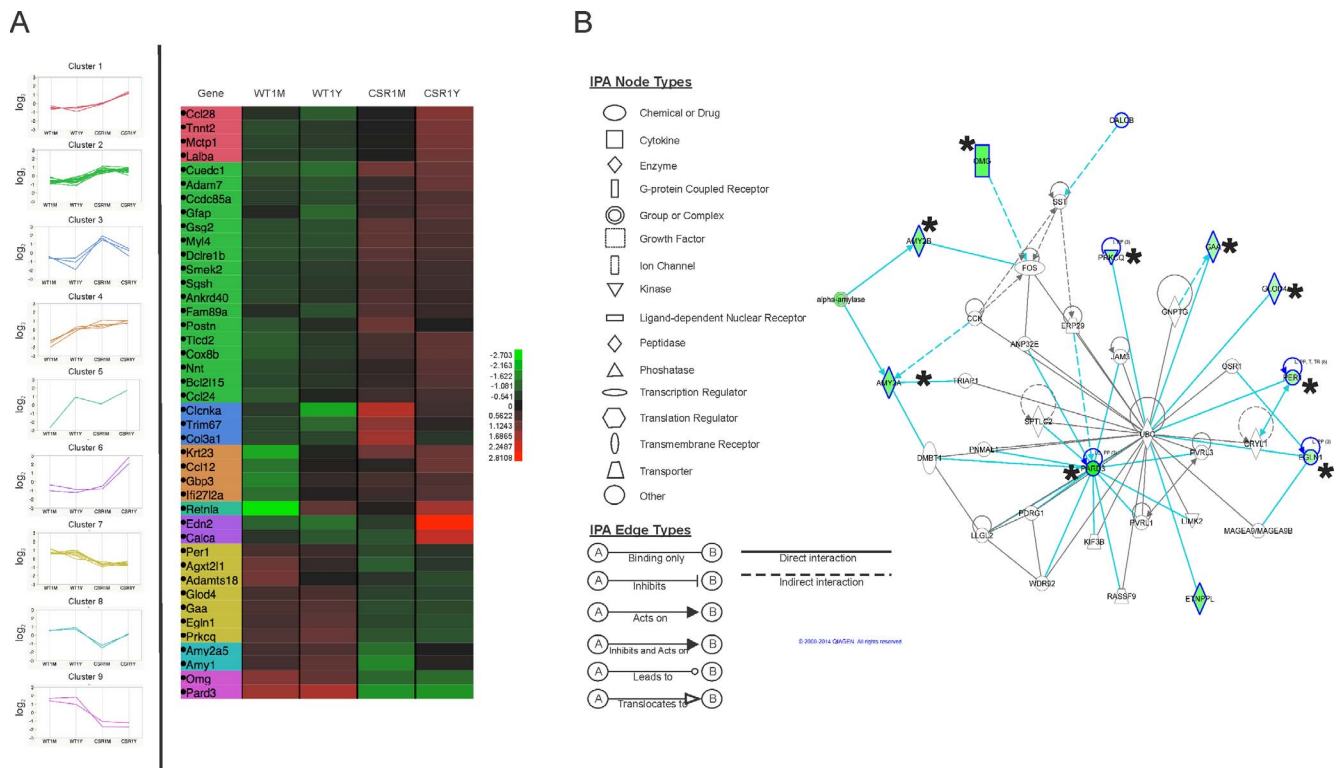


**FIGURE 8.** (A) A heat map exhibiting the behavior of the 42 genes meeting our criteria for a statistically significant expression change between age-matched WT (WT1M, WT1Y) and rpe1 (CSR1M, CSR1Y) mice. Genes that behave similarly are clustered together into nine groups with their log<sub>2</sub>-fold change shown in the column of graphs on the left. A reference scale from the log<sub>2</sub>-fold change represented by colors in the heat map is shown on the right. Visual inspection of the heat map shows the clear segregation of the expression of the genes into the WT and mutant groups. It also shows that many more genes are upregulated (red) than downregulated (green). Gene clusters 1, 2, 4, 5, 7, and 9 are generally consistent in their changes between the P30 (WT1M, CSR1M) and P365 (WT1Y, CSR1Y) animals, while those in cluster 3 show first up, then downregulation, while those in cluster 8 show the opposite trend. (B) A gene network generated by IPA using genes identified by microarray data as downregulated (green) as well as inferred genes involved (ubiqite) in the rpe1 mouse. Genes that showed statistically significant change in the rpe1 mouse are denoted by an asterisk. The network emphasizes the significant impact of the mutation on fundamental cellular processes: regulatory (CALCB, PRKCQ, PER1, EGLN1, SST, FOS, CCK, GNPTG, OSR1, ANP32E, TRIAP1, UBC, LNMAL1, DMBT1, PDRG1, LIMK2, MageA9, RASSF9, WDR92); metabolic (AMY2A, AMY2B, GAA, GLOD4, ETNPPL/AGXT2L1, ERP29, SPTLC2, CRYL1); intracellular molecular transport (KIF3B); and establishing intracellular junctions (PARD3, JAM3, PVRL3, PVRL1), cell adhesion (OMG, PVRL1), and cell polarity (PARD3, LLGL2).

choroidal blood vessels in some complex way but that it may be independent of the initial production of a detachment.

The mutation affects a large variety of metabolism-related genes, and mitochondria in both the retina and RPE are abnormal in structure and number. The movement of water from the retina, across the RPE and into the choroid is an energy dependent process,<sup>47</sup> thus a defect of energy metabolism may contribute to fluid accumulation in the SRS. Downregulation of *Adamts18* may be associated with abnormalities of the extracellular matrix and thus be one of the factors producing an increased susceptibility to the formation or expansion of SRDs. The *Pard3* gene is highly significant because of its known involvement in establishing the polarity of epithelial cells and formation of junctional complexes. It has also been shown to be associated with tight-junction formation between capillary endothelial cells in the brain.<sup>37</sup>

The other major change in the mutant based on combined microarray and qRT-PCR data, as well as IPA analysis (October 2014), is in the expression of the *Prckq* gene. Its gene product, *PKCθ*, is a non-Ca<sup>2+</sup>-dependent member of the PKC family and is implicated in a wide variety of cellular functions.<sup>48,49</sup> Indeed Ji et al.<sup>15</sup> recently reported that the gene defect in the rpe1 strain is a result of a mutation at the splice donor site leading to a frameshift, that produces a stop codon. They described changes in proteins associated with

the junctional complex of RPE cells congruent with the data reported here. Variants of the PKC family have been shown to play a significant role in the assembly and maintenance of tight junctions through the phosphorylation of the tight-junction protein occludin. Abnormal expression of junctional proteins, as well as PKCθ's known involvement in the suppression of the ERK pathway with an effect on fluid transport across the RPE may suggest a direct mechanism for the formation of SRDs in this mutant.<sup>50,51</sup> It has been demonstrated that PKCθ is involved in regulating the formation of junctional complexes and changes in the permeability of the blood-brain barrier and intestinal epithelia.<sup>52-54</sup> *Pard3*'s direct effect on cell polarity and junctional complexes may implicate it as the most direct player in SRD production in this mutant with *Prckq* acting as an upstream regulator. Thus, our data provides additional evidence that the mutation may have multiple effects on RPE cells, including changes in the expression of proteins associated with adhering junctions, tight junctions, and microvilli. Structural changes include the loss of apical microvilli and a reversal of structural polarity in many cells. These abnormal cells may lose their ability to dehydrate the subretinal space or even show a reversal of directional fluid transport across the monolayer, either of which could result in the production of a serous detachment. Other studies have suggested that sublethal oxidative stress, aging, or the

TABLE 3. 20 Canonical Pathways Affected in the rpe1 Retina

Canonical Pathways Affected by Upregulated Genes in rpe1 Mice	Functional Effects	Genes
Agranulocyte Adhesion and Diapedesis	Immune/Inflammation	GFAP, MYL4, PARD3
Granulocyte Adhesion and Diapedesis	Immune/Inflammation	CCL12, CCL24, CCL28
Chemokine Signaling	Immune/Inflammation	CCL12, CCL24
Calcium Signaling	Signaling	MYL4, TNNT2
Signaling by Rho Family GTPases	Cytoskeleton	GFAP, MYL4, PARD3
IL-17A Signaling in Fibroblasts	Immune/Inflammation	CCL12
MSP-ROn Signaling Pathway	Vasculature	CCL12
IL-17A Signaling in Fibroblasts	Immune/Inflammation	CCL12
Intrinsic Prothrombin Activation Pathway	Vasculature	Col3A1
Differential Regulation of Cytokine Production in Macrophages and T Helper Cells by IL-17A and IL-17F	Immune/Inflammation	CCL12
Canonical Pathways Affected by Downregulated Genes in rpe1 Mice	Functional Effects	Genes
HER-2 Signaling in Breast Cancer	Growth Factor Signaling	PARD3, PRKCQ
Glycogen Degradation III	Metabolism	GAA
UVC-Induced MAPK Signaling	Signaling	PRKCQ
nNOS Signaling in Neurons	Ach R Aggregation	PRKCQ
UVB-Induced MAPK Signaling	Signaling	PRKCQ
Thrombopoietin Signaling	Signaling	PRKCQ
Calcium-induced T-Lymphocyte Apoptosis	Immune/Inflammation	PRKCQ
Erythropoietin Signaling	Vasculature	PRKCQ
CCR5 Signaling in Macrophages	Immune/Inflammation	PRKCQ
Growth Hormone Signaling	Immune/Inflammation	PRKCQ

misdirected trafficking of critical transport molecules lead to changes in the structural and physiological polarity of the RPE.<sup>55</sup> Indeed, transduction of the RPE by an adenovirus-cystic fibrosis transmembrane conductance regulator (AV-CFTR) construct produces a change in the localization of this transport molecule so that it is overexpressed on the apical membrane. This change in localization results in a reversal of fluid flow such that the RPE secretes fluid into the subretinal space instead of absorbing fluid from it.<sup>56</sup>

Our data provide additional evidence that the newly described rpe1a mutation produces many important changes in the retina, especially in the RPE and its interface with the neural retina. Many of these changes suggest mechanisms that may affect retinal adhesion ultimately leading to the production of serous retinal detachment. The information presented here can be used in subsequent studies to more precisely determine the role of PKC $\theta$  in RPE function and perhaps its role in the formation of serous-type retinal detachments.

### Acknowledgments

The authors thank the large number of dedicated University of California at Santa Barbara undergraduate students who helped in the preparation of tissue samples for this project.

Supported by Macula Vision Research Foundation, Santa Barbara Cottage Hospital, National Science Foundation (IIS-0808772, ITR-0331697).

Disclosure: **G. Luna**, None; **G.P. Lewis**, None; **K.A. Linberg**, None; **B. Chang**, None; **Q. Hu**, None; **P.J. Munson**, None; **A. Maminishkis**, None; **S.S. Miller**, None; **S.K. Fisher**, None

### References

- Forster DJ, Cano MR, Green RL, Rao NA. Echographic features of the Vogt-Koyanagi-Harada syndrome. *Arch Ophthalmol*. 1990;108:1421-1426.
- Song JH, Bae JH, Rho MI, Lee SC. Intravitreal bevacizumab in the management of subretinal fluid associated with choroidal osteoma. *Retina*. 2010;30:945-951.
- Bird AC, Hamilton AM. Placoid pigment epitheliopathy. Presenting with bilateral serous retinal detachment. *Br J Ophthalmol*. 1972;56:881-886.
- Anand R, Tasman WS. Nonrhegmatogenous retinal detachment. In: Wilkinson CP, ed. *Retina*. Vol. 3. Philadelphia, PA: Elsevier; 2006:2121-2141.
- Nicholson B, Noble J, Forooghian F, Meyerle C. Central serous chorioretinopathy: update on pathophysiology and treatment. *Surv Ophthalmol*. 2013;58:103-126.
- van Velthoven MEJ, Verbraak FD, Garcia PM, Schlingemann RO, Rosen RB, de Smet MD. Evaluation of central serous retinopathy with en face optical coherence tomography. *Br J Ophthalmol*. 2005;89:1483-1488.
- Bird AC. Pathogenesis of serous detachment of the retina and pigment epithelium. In: Wilkinson CP, ed. *Retina*. Vol. 3. Philadelphia, PA: Elsevier; 2006:971-977.

8. Marmor MF. Mechanisms of normal retinal adhesion. In: Ryan SJ, Wilkinson CP, eds. *Retina*. St. Louis, MO: Elsevier; 2006: 1891-1908.
9. Marmor MF, Abdul-Rahim AS, Cohen DS. The effect of metabolic inhibitors on retinal adhesion and subretinal fluid resorption. *Invest Ophthalmol Vis Sci*. 1980;19:893-903.
10. Marmor MF, Maack T. Local environmental factors and retinal adhesion in the rabbit. *Exp Eye Res*. 1982;34:727-733.
11. Marmor MF. Mechanisms of retinal adhesion. *Prog Retin Res*. 1993;12:179-204.
12. Johnson LV, Hageman GS. Structural and compositional analyses of isolated cone matrix sheaths. *Invest Ophthalmol Vis Sci*. 1991;32:1951-1957.
13. Yao XY, Hageman GS, Marmor MF. Retinal adhesiveness is weakened by enzymatic modification of the interphotoreceptor matrix in vivo. *Invest Ophthalmol Vis Sci*. 1990;31:2051-2058.
14. Hageman GS, Marmor MF, Yao XY, Johnson LV. The interphotoreceptor matrix mediates primate retinal adhesion. *Arch Ophthalmol*. 1995;113:655-660.
15. Ji X, Liu Y, Hurd R, et al. Retinal pigment epithelium atrophy 1 (rpea1): a new mouse model with retinal detachment caused by a disruption of protein kinase C,  $\theta$ . *Invest Ophthalmol Vis Sci*. 2016;57:877-888.
16. Ober MD, Yannuzzi LA, Do DV, et al. Photodynamic therapy for focal retinal pigment epithelial leaks secondary to central serous chorioretinopathy. *Ophthalmology*. 2005;112:2088-2094.
17. Luna G, Kjellstrom S, Verardo MR, et al. The effects of transient retinal detachment on cavity size and glial and neural remodeling in a mouse model of X-linked retinoschisis. *Invest Ophthalmol Vis Sci*. 2009;50:3977-3984.
18. Lewis GP, Chapin EA, Luna G, Linberg KA, Fisher SK. The fate of Müller's glia following experimental retinal detachment: nuclear migration, cell division, and subretinal glial scar formation. *Mol Vis*. 2010;16:1361-1372.
19. Karnovsky MJ. A formaldehyde-glutaraldehyde fixative of high osmolality for use in electron microscopy. *J Cell Biol*. 1965;27: 137A.
20. Johnson PT, Betts KE, Radeke MJ, Hageman GS, Anderson DH, Johnson LV. Individuals homozygous for the age-related macular degeneration risk-conferring variant of complement factor H have elevated levels of CRP in the choroid. *Proc Natl Acad Sci U S A*. 2006;103:17456-17461.
21. Luna G, Lewis GP, Banna CD, Skalli O, Fisher SK. Expression profiles of nestin and synemin in reactive astrocytes and Müller cells following retinal injury: a comparison with glial fibrillar acidic protein and vimentin. *Mol Vis*. 2010;16:2511-2523.
22. Massah S, Hollebakk R, Labrecque MP, Kolybaba AM, Beischlag TV, Prefontaine GG. Epigenetic characterization of the growth hormone gene identifies SmcHD1 as a regulator of autosomal gene clusters. Feil R, ed. *PLoS One*. 2014;9:e97535.
23. Radeke MJ, Peterson KE, Johnson LV, Anderson DH. Disease susceptibility of the human macula: differential gene transcription in the retinal pigmented epithelium/choroid. *Exp Eye Res*. 2007;85:366-380.
24. Vandesompele J, De Preter K, Pattyn F, et al. Accurate normalization of real-time quantitative RT-PCR data by geometric averaging of multiple internal control genes. *Genome Biol*. 2002;3:RESEARCH0034.
25. Chen J, Qian H, Horai R, Chan C-C, Caspi RR. Use of optical coherence tomography and electroretinography to evaluate retinal pathology in a mouse model of autoimmune uveitis. *PLoS One*. 2013;8:e63904.
26. Lewis GP, Sethi CS, Linberg KA, Charteris DG, Fisher SK. Experimental retinal reattachment: a new perspective. *Mol Neurobiol*. 2003;28:159-175.
27. Lewis GP, Linberg KA, Fisher SK. Neurite outgrowth from bipolar and horizontal cells after experimental retinal detachment. *Invest Ophthalmol Vis Sci*. 1998;39:424-434.
28. Rattner A, Nathans J. The genomic response to retinal disease and injury: evidence for endothelin signaling from photoreceptors to glia. *J Neurosci*. 2005;25:4540-4549.
29. Cheng CL, Molday RS. Changes in gene expression associated with retinal degeneration in the rd3 mouse. *Mol Vis*. 2013;19: 955-969.
30. Bordeleau F, Bessard J, Marceau N, Sheng Y. Measuring integrated cellular mechanical stress response at focal adhesions by optical tweezers. *J Biomed Opt*. 2011;16(9):095005-095008.
31. Hiscott P, Sheridan C, Magee RM, Grierson I. Matrix and the retinal pigment epithelium in proliferative retinal disease. *Prog Retin Eye Res*. 1999;18:167-190.
32. Paudel S, Kim YH, Huh M-I, et al. ADAM10 mediates N-cadherin ectodomain shedding during retinal ganglion cell differentiation in primary cultured retinal cells from the developing chick retina. *J Cell Biochem*. 2013;114:942-954.
33. Yan X, Lin J, Rolfs A, Luo J. Differential expression of the ADAMs in developing chicken retina. *Dev Growth Differ*. 2011;53:726-739.
34. Sel S, Kalinski T, Enssen I, et al. Expression analysis of ADAM17 during mouse eye development. *Ann Anat*. 2012;194:334-338.
35. Goldstein O, Mezey JG, Boyko AR, et al. An ADAM9 mutation in canine cone-rod dystrophy 3 establishes homology with human cone-rod dystrophy 9. *Mol Vis*. 2010;16:1549-1569.
36. You J-J, Yang C-H, Yang C-M, Chen M-S. Cyr61 induces the expression of monocyte chemoattractant protein-1 via the integrin  $\alpha v \beta 3$ , FAK, PI3K/Akt, and NF- $\kappa B$  pathways in retinal vascular endothelial cells. *Cell Signal*. 2014;26:133-140.
37. Artus C, Glacial F, Ganeshamoorthy K, et al. The Wnt/planar cell polarity signaling pathway contributes to the integrity of tight junctions in brain endothelial cells. *J Cereb Blood Flow Metab*. 2014;34:433-440.
38. Fisher SK, Lewis GP, Linberg KA, Verardo MR. Cellular remodeling in mammalian retina: results from studies of experimental retinal detachment. *Prog Retin Eye Res*. 2005; 24:395-431.
39. Cook B, Lewis GP, Fisher SK, Adler R. Apoptotic photoreceptor degeneration in experimental retinal detachment. *Invest Ophthalmol Vis Sci*. 1995;36:990-996.
40. Mervin K, Valter K, Maslim J, Lewis G, Fisher S, Stone J. Limiting photoreceptor death and deconstruction during experimental retinal detachment: the value of oxygen supplementation. *Am J Ophthalmol*. 1999;128:155-164.
41. Lazarus HS, Hageman GS. Xyloside-induced disruption of interphotoreceptor matrix proteoglycans results in retinal detachment. *Invest Ophthalmol Vis Sci*. 1992;33:364-376.
42. Hayashi H, Tamura A, Krishnan D, et al. Ezrin is required for the functional regulation of the epithelial sodium proton exchanger, NHE3. *PLoS One*. 2013;8:e55623.
43. Murad N, Kokkinaki M, Gunawardena N, et al. miR-184 regulates ezrin, LAMP-1 expression, affects phagocytosis in human retinal pigment epithelium and is downregulated in age-related macular degeneration. *FEBS J*. 2014;281:5251-5264.
44. Edelman JL, Lin H, Miller SS. Acidification stimulates chloride and fluid absorption across frog retinal pigment epithelium. *Am J Physiol*. 1994;266(Pt 1):C946-C956.
45. Viswanatha R, Bretscher A, Garbett D. Dynamics of ezrin and EBP50 in regulating microvilli on the apical aspect of epithelial cells. *Biochem Soc Trans*. 2014;42:189-194.
46. García-Ponce A, Citalán-Madrid AF, Velázquez-Avila M, Vargas-Robles H, Schnoor M. The role of actin-binding proteins in the control of endothelial barrier integrity. *Thromb Haemost*. 2015;113:20-36.

47. Peterson WM, Meggyesy C, Yu K, Miller SS. Extracellular ATP activates calcium signaling, ion, and fluid transport in retinal pigment epithelium. *J Neurosci.* 1997;17:2324-2337.
48. Kim JK, Fillmore JJ, Sunshine MJ, et al. PKC-theta knockout mice are protected from fat-induced insulin resistance. *J Clin Invest.* 2004;114:823-827.
49. Meller N, Liu YC, Collins TL, et al. Direct interaction between protein kinase C theta (PKC theta) and 14-3-3 tau in T cells: 14-3-3 overexpression results in inhibition of PKC theta translocation and function. *Mol Cell Biol.* 1996;16:5782-5791.
50. Omri S, Behar-Cohen F, Rothschild P-R, et al. PKC $\zeta$  mediates breakdown of outer blood-retinal barriers in diabetic retinopathy. *PLoS One.* 2013;8:e81600.
51. Marino JS, Hinds TD, Potter RA, et al. Suppression of protein kinase C theta contributes to enhanced myogenesis in vitro via IRS1 and ERK1/2 phosphorylation. *BMC Cell Biol.* 2013;14:39.
52. Willis CL, Meske DS, Davis TP. Protein kinase C activation modulates reversible increase in cortical blood-brain barrier permeability and tight junction protein expression during hypoxia and posthypoxic reoxygenation. *J Cereb Blood Flow Metab.* 2010;30:1847-1859.
53. Banan A, Zhang LJ, Shaikh M, Fields JZ, Farhadi A, Keshavarzian A. Theta-isoform of PKC is required for alterations in cytoskeletal dynamics and barrier permeability in intestinal epithelium: a novel function for PKC-theta. *Am J Physiol, Cell Physiol.* 2004;287:C218-C234.
54. Banan A, Zhang LJ, Shaikh M, et al. theta Isoform of protein kinase C alters barrier function in intestinal epithelium through modulation of distinct claudin isotypes: a novel mechanism for regulation of permeability. *J Pharmacol Exp Ther.* 2005;313:962-982.
55. Burke JM. Epithelial phenotype and the RPE: is the answer blowing in the Wnt? *Prog Retin Eye Res.* 2008;27:579-595.
56. Peterson WM, Quong JM, Miller SS. Mechanisms of fluid transport in retinal pigment epithelium. The Third Great Basin Visual Science Symposium. Vol. 3; 1998:34-42.